Phase-field lattice kinetic scheme for the numerical simulation of dendritic growth

I. Rasin* and W. Miller
Institute for Crystal Growth (IKZ), Max-Born-Strasse 2, 12489 Berlin, Germany

S. Succi
Istituto Applicazioni Calcolo CNR, 137 Viale del Policlinico, 00144 Rome, Italy
(Received 16 March 2005; published 28 December 2005)

A phase-field lattice kinetic model is presented for the numerical simulation of the dendritic growth of a pure crystal in the presence of thermal transport. A finite-difference scheme for the phase field is combined with an explicit lattice kinetic scheme for the temperature field. The resulting scheme is advanced in time with an adaptive time-marching procedure which permits us to achieve long simulation times with larger time steps than explicit finite-difference and previous kinetic methods. The method is demonstrated for the case of dendritic growth of a single crystal over a wide range of Stefan and capillarity numbers.

DOI: 10.1103/PhysRevE.72.066705 PACS number(s): 68.70.+w, 44.05.+e

I. INTRODUCTION

In the recent past, phase-field methods have rapidly emerged as the tool of choice for the numerical simulation of interfacial phenomena in solidification processes [1–6]. The major advantage of the phase-field method is to avoid the explicit tracking of thin and often quite complex interfaces. This is achieved by introducing a real-valued order parameter, or phase field, whose asymptotic values, typically 0 and 1, tell fluid and solid phases apart. The interface between solid and liquid phases is then identified as the region where the phase field switches between the values characterizing the two phases. However, a potential drawback of the phase-field method is that very high resolution is needed to resolve the interface accurately. The resolution problem has a particularly severe impact on the time span of the simulation, especially if explicit time stepping is used for the diffusive terms. A common way to circumvent time-step limitations is to turn to implicit time marching. This removes the stability constraint (not the accuracy ones, though) but at the price of being forced to solve an expensive matrix problem at each time step. Another, more sophisticated, option is dynamic grid refinement [4], in which mesh resolution is dynamically adapted to the growing interface. This is possibly the most efficient strategy, but it comes at the cost of significant complications in the code structure.

In this paper, we present an option that permits us to achieve large time steps without surrendering the simplicity of explicit formulations. This is accomplished by a kinetic representation of the heat conduction equation. By kinetic, we mean that diffusion is not represented directly by a second order space derivative, but rather emerges as an adiabatic limit of a relaxation-propagation dynamics of underlying (computational) particles [7–9]. The advantage of such a representation is that space and time derivatives always appear at the same (first) order, so that the Courant-Friedrichs-Lewy (CFL) stability constraints imply a linear scaling of the time step with the mesh spacing, as opposed to the quadratic scaling of standard explicit methods. In addition, conservation laws can be enforced into the schemes to machine roundoff precision. In this paper, we present a kinetic method allowing for a variable time step which can be adapted to the actual time scale of the physical problem in the course of the evolution. The method offers enhanced efficiency without requiring any major change in the algorithmic structure of the computational scheme. Moreover, the present kinetic method naturally accommodates anisotropic and inhomogeneous diffusion coefficients, which play a major role in the crystallization of materials with different heat diffusivity in the two phases.

II. GOVERNING EQUATIONS

The physical problem we are going to address is the simulation of crystallization processes from pure materials. This involves two scalar fields, the phase field ϕ, distinguishing between liquid and solid phases, and the temperature field T.

The governing equation for the phase-field model is

$$\tau\partial_t\phi = \xi^2\Delta\phi - g_\phi - \lambda p_\phi \tilde{T}, \tag{1}$$

where $\phi=0$ denotes the liquid and $\phi=1$ the solid phase.

The temperature equation reads

$$\partial_t T = D_T\Delta T + \frac{L}{c_p}\partial_t h(\phi), \tag{2}$$

where $\tilde{T}\equiv T-T_m$, T_m being the melting-point temperature.

In the above, ξ is a measure of the interface width, τ is a characteristic relaxation time of the phase field, and λ is a measure of the coupling between thermal and diffusive effects. D_T is the thermal diffusivity, and L and c_p are the latent heat and heat capacity, respectively. The subscript ϕ stands for the partial derivative with respect to ϕ. The term $g(\phi)$ is an arbitrary function with minima in the stable phases. It is usually taken in the form of a double-well potential:

$$g(\phi) = \phi^2(1-\phi)^2. \tag{3}$$

*Present address: Department of Chemical Engineering, Technion, Haifa, 32000, Israel; electronic address: irasin@tx.technion.ac.il

TABLE I. Different expressions for $h(\phi)$.

$h(\phi)$	a_2
ϕ	0.5539
$10\phi^3-15\phi^4+6\phi^5$	0.3519

The term $p(\phi)$ is a monotone function in the interval [0, 1] and takes values 0 and 1 on the left and right boundaries, respectively. It is taken as a polynomial of the fifth order for stability reasons:

$$p=\phi^3(6\phi^2-15\phi+10). \tag{4}$$

Usually the function $h(\phi)$ is also taken in the form of a polynomial with the same conditions as for $p(\phi)$. It was shown in [10] that in order for the model to be thermodynamically consistent $h(\phi)$ should be equal to $p(\phi)$, but other polynomials can also be used [5]. The expressions used for $h(\phi)$ are listed in Table I.

The above equations describe the phase boundary which moves according to the Gibbs-Thomson and growth kinetic effects. Its velocity is given by

$$V=-\mu\left(\frac{Ld_0}{c_pR}+\tilde{T}\right), \tag{5}$$

where R is the local radius of curvature, μ is the kinetic coefficient, and $d_0=\gamma_0 T_m c_p/L^2$, γ_0 being the surface tension, is the capillary length.

The parameters ξ, τ, and λ are related to the physical properties through the following expressions:

$$\mu^{-1}=a_1\frac{\tau}{\lambda\xi}-a_2\frac{\xi L}{D_T c_p}, \tag{6}$$

$$d_0=a_1\frac{\xi c_p}{\lambda L}, \tag{7}$$

$$w=\xi/a_1, \tag{8}$$

where w is the width of the transition region, $a_1=1/3\sqrt{2}$ and values of a_2 are listed in Table I. It is convenient to introduce the capillary length number Ca as the ratio between the capillary length d_0 and the characteristic length of the transition region:

$$\mathrm{Ca}=\frac{d_0}{\xi}. \tag{9}$$

The limit $\mathrm{Ca}\to\infty$ characterizes the regime of zero-thickness interfaces. Small capillary length numbers are associated with "thick" interfaces which allow low numerical resolution. Thus, the capillary length number should be kept as small as possible, compatibly with the need of resolving the physical length scales, typically the tip radius R. A second major control parameter is the dimensionless undercooling, or Stefan number, defined as

$$\mathrm{St}=c_p(T_m-T_0)/L, \tag{10}$$

where T_0 is the asymptotic temperature at an infinitely remote boundary. Small Stefan numbers are computationally demanding because they correspond to very slow evolutions toward steady state.

III. KINETIC FINITE-DIFFERENCE SCHEME FOR HEAT TRANSPORT

The solution of the phase-field temperature equations in d dimensions involves of the order of $N_{DOF}\sim(l/w)^d$ spatial degrees of freedom, where $l=D_T/V$ is a typical macroscopic diffusion length. The corresponding time span of the simulation is of the order of $N_t=l^2/D_T\tau$ time steps of size $\delta t=w/V$, which leads to a computational load scaling like $(l/w)^{d+2}$. Typical values under ordinary undercooling conditions $(0.1<\mathrm{St}<1)$ easily lead to several millions of time steps. At lower undercooling, the tip velocity becomes correspondingly smaller and the time-step problem increasingly more demanding. This provides a strong motivation toward the development of fast or long time steppers.

Kinetic methods (KMs) offer an appealing perspective in this direction. In particular, since they allow the time step to scale linearly with the mesh size, they offer a better computational load, scaling like $(l/w)^{d+1}$.

The main idea of the kinetic methods is to introduce a distribution function $f(\vec{r},\vec{v})$ of quasiparticles in phase space $(\vec{r},\vec{v})$. For the purpose of reproducing hydrodynamic diffusion it is sufficient to retain only a very limited number of discrete velocities $\vec{c}_i$. In fact, in d dimensions, $2d$ discrete speeds are sufficient to recover hydrodynamic diffusion.

The notation $f_i(\vec{r})$ is chosen for the discrete distribution functions, where the index i corresponds to velocity space $\vec{c}_i$, and $\vec{r}$ labels the spatial node in the discrete grid. The most common form of discrete kinetic equation is [11,12]

$$f_i(\vec{r}+\vec{c}_i\delta t,t+\delta t)=f_i(\vec{r},t)-\sum_j \Omega_{ij}\delta t[f_j(\vec{r},t)-f_j^{eq}(\vec{r},t)], \tag{11}$$

where Ω_{ij} is a relaxation matrix and f_j^{eq} is a local equilibrium distribution. The physical observables are defined through simple summations over the velocity degrees of freedom. In the case of the heat equation, the temperature and the heat flux are defined as follows:

$$T=\sum_i f_i, \quad J_\alpha=\sum_i c_{i\alpha}f_i, \tag{12}$$

where greek indices label Cartesian space coordinates. Pictorially, we can think of f as the distribution of "phonons", whose density and current density correspond to the thermal energy (temperature) and thermal flux of the melt, respectively. Here we consider a four-speed velocity space defined by the four discrete speeds connecting each lattice site to its nearest neighbors (in units of $\delta x/\delta t$):

$$\vec{c}_1=(1,0), \quad \vec{c}_2=(0,1), \quad \vec{c}_3=(-1,0), \quad \vec{c}_4=(0,-1). \tag{13}$$

In two dimensions, the matrix Ω_{ij} has the following eigenvectors [7]:

$$V^{(0)}=(1,1,1,1), \quad V^{(1)}=(1,0,-1,0),$$

$$V^{(2)} = (0,1,0,-1), \quad V^{(3)} = (1,-1,1,-1). \tag{14}$$

The corresponding collision matrix can be constructed according to the spectral-decomposition rule [13,14]:

$$\Omega_{ij} = w_i \sum_{k=1}^{4} \omega_k \frac{V_i^{(k)} V_j^{(k)}}{N_k}, \tag{15}$$

where $N_k = \Sigma_i V_i^{(k)} w_i V_i^{(k)}$ are normalization factors, w_i is a set of weights, $w_i = 1/4$, and ω_k are (non-negative) eigenvalues which encode relaxation to local equilibria and control the diffusion parameters. For the case of a fluid flow with velocity $\vec{u}$, the equilibrium populations f_i^{eq} are chosen as follows [7]:

$$f_i^{eq} = w_i T \left(1 + \frac{\vec{c}_i \cdot \vec{u}}{c_s^2} \right), \tag{16}$$

where $c_s^2 = \Sigma w_i c_{ix}^2 = \Sigma w_i c_{iy}^2 = 1/2$ is the sound speed of the lattice. However, hereafter we shall focus on the case of no flow, $\vec{u} = \vec{0}$. With this choice, the equilibrium expressions for the kinetic moments $P_{\alpha\beta}$ and $Q_{\alpha\beta\gamma}$ (see next section) take the following form:

$$P_{\alpha\beta}^{eq} = c_s^2 T \delta_{\alpha\beta}, \quad Q_{\alpha\beta\gamma}^{eq} = 0, \quad R_{\alpha\beta\gamma\delta}^{eq} = 0.$$

A. Diffusion via adiabatic approximation

In the kinetic approach diffusion is not represented directly by second order spatial derivatives, but rather as an emergent property from propagation-relaxation dynamics. In order to appreciate this point, the first step is to split the distribution function into equilibrium and nonequilibrium components, and then assume that the latter be a small perturbation of the former:

$$f_i = f_i^{eq} + f_i^{ne}, \quad f_i^{ne} \sim \epsilon f_i^{eq},$$

where ϵ is a smallness parameter, typically the ratio of molecular mean free path to the smallest macroscopic length (Knudsen number).

The adiabatic approximation implies the following relations for the physical values:

$$\frac{\omega_J \dot{J}_x}{J_x} \ll 1, \quad \frac{\omega_J \dot{J}_y}{J_y} \ll 1, \quad \frac{\omega_P \dot{P}_{\alpha\beta}}{P_{\alpha\beta}} \ll 1, \tag{17}$$

where we have set $\omega_1 = 0$ (by mass conservation), $\omega_J \equiv \omega_2 = \omega_3$, and $\omega_P \equiv \omega_4$.

To see how the kinetic equation (11) reproduces the diffusion equation in the adiabatic limit $\partial_t f \ll \omega f$, we first expand the streaming term at the left hand side to second order in the lattice time step δt:

$$\partial_t f_i + c_{i\alpha}\partial_\alpha f_i + \delta t \left(\frac{1}{2}\partial_{tt} f_i + c_{i\alpha}\partial_{t\alpha} f_i + \frac{c_{i\alpha}c_{i\beta}}{2}\partial_{\alpha\beta} f_i \right) = \sum_j \Omega_{ij}(f_j^{eq} - f_j). \tag{18}$$

Subsequently, we take moments of the expanded equation, that is, we sum over $\Sigma_i \Psi_i$, with $\Psi_i = \{1, c_{i\alpha}, c_{i\alpha}c_{i\beta}\}$. This leads to the following set of partial differential equations:

$$F + \frac{\delta t}{2}(\partial_t F + \partial_\alpha F_\alpha) = 0,$$

$$F_\alpha + \frac{\delta t}{2}(\partial_t F_\alpha + \partial_\beta F_{\alpha\beta}) = -\omega_J J_\alpha,$$

$$F_{\alpha\beta} + \frac{\delta t}{2}(\partial_t F_{\alpha\beta} + \partial_\gamma F_{\alpha\beta\gamma}) = -\omega_P (P_{\alpha\beta} - P_{\alpha,\beta}^{eq}),$$

where we have defined the following differential one-forms:

$$F \equiv \partial_t T + \partial_\alpha J_\alpha,$$

$$F_\alpha \equiv \partial_t J_\alpha + \partial_\beta P_{\alpha\beta},$$

$$F_{\alpha\beta} \equiv \partial_t P_{\alpha\beta} + \partial_\gamma Q_{\alpha\beta\gamma},$$

$$F_{\alpha\beta\gamma} \equiv \partial_t Q_{\alpha\beta\gamma} + \partial_\delta R_{\alpha\beta\gamma\delta},$$

and tensorial kinetic moments:

$$P_{\alpha\beta} \equiv \sum_i f_i c_{i\alpha} c_{i\beta},$$

$$Q_{\alpha\beta\gamma} \equiv \sum_i f_i c_{i\alpha} c_{i\beta} c_{i\gamma},$$

$$R_{\alpha\beta\gamma\delta} \equiv \sum_i f_i c_{i\alpha} c_{i\beta} c_{i\gamma} c_{i\delta}.$$

Since we have only four discrete speeds, the only nonzero components of the above kinetic tensors are $P_{xx}, Q_{xxx} = c_s^2 T J_x, R_{xxxx} = c_s^2 P_{xx}$, and the same by exchanging x with y.

To leading order in δt, the above set of tensorial equations reduces to the following:

$$F = 0,$$

$$F_\alpha = -\omega_J J_\alpha,$$

$$F_{\alpha\beta} = -\omega_P (P_{\alpha\beta} - P_{\alpha,\beta}^{eq}).$$

The second relation yields $J_\alpha = -F_\alpha/\omega_J$, which, inserted into the first one, delivers

$$\partial_t T - \frac{1}{\omega_J}[\partial_\alpha(\partial_t J_\alpha + \partial_\beta P_{\alpha\beta})] = 0.$$

Next, by adiabaticity, we shall assume that $\partial_t J_\alpha \ll \omega_J J_\alpha$ and $P_{\alpha\beta} \sim P_{\alpha\beta}^{eq} = T c_s^2 \delta_{\alpha\beta}$. This leaves us with

$$\partial_t T = \frac{c_s^2}{\omega_J}\partial_{\alpha\alpha} T,$$

which is the desired diffusion equation, with a diffusivity $D_T = c_s^2/\omega_J$. This quick derivation can be made more rigorous by taking into account terms up to second order in the time step δt. The final result is the following telegrapher's equation:

$$\partial_t \left(T + \frac{\delta t}{2}\partial_t T \right) = c_s^2 (1/\omega_J - \delta t/2)\partial_{\alpha\alpha} T + O(\delta t)^2.$$

By assuming $\delta t \partial_{tt} T \ll \partial_t T$, we are left with a diffusion equation with a renormalized diffusivity

$$D_T = c_s^2(1/\omega_J - \delta t/2). \tag{19}$$

The second term on the right hand side, sometimes called propagation diffusivity, is a typical signature of kinetic schemes, for it derives from the second order expansion of the streaming term in the kinetic equation. A Fourier analysis shows in fact that the scheme is linearly stable under the CFL condition [12]

$$0 < \omega_J \delta t < 2, \tag{20}$$

$$c\,\delta t \leqslant \delta x. \tag{21}$$

The first inequality stems from the explicit (forward Euler) time integration of the collision operator, and it is seen to coincide with the condition that the diffusivity D_T be positive definite. The second one stems from the CFL requirement on the streaming operator, which is integrated *exactly*, since the discrete speeds are constant in space and time. Since in the kinetic scheme the particles move along the light cones defined by the condition $c\,\delta t = \delta x$, the second CFL condition is satisfied by default.

It should be noted that the lattice kinetic method in d dimensions requires $2d$ discrete distribution functions, thereby introducing a memory overhead which has to be weighted against the gain in the size of the time step.

IV. ADAPTIVE TIME STEPPING

A major computational advantage of lattice kinetic methods, as compared to other particle methods, is that particles move along a set of constant and prescribed directions defined by the discrete speeds $\vec{c}_i$. By choosing the time step according to the light-cone condition $c\,\delta t = \delta x$, particle dynamics takes place entirely on the lattice. This is a significant computational advantage, since no interpolation is required to locate the particles in the spatial grid. On the other hand, the price is that the mesh must necessarily be uniform and the time step cannot be changed in time unless the mesh spacing is changed accordingly (as is done in multiscale kinetic methods). The latter limitation is particularly severe for situations like the one discussed previously, in which long simulation times are required. In the following, we show how the time-step limitation can be circumvented by a proper rescaling (or *annealing*) of the discrete velocities. The scope of dynamic time stepping is to adapt the time-step size to the actual change rate of the relevant physical quantities without changing the spatial grid resolution.

With reference, say, to the flux J, let us introduce the *diabatic* parameter ϵ_J:

$$\epsilon_J \equiv \frac{(\delta t\, \partial J^{eq}/\partial t)}{\omega_J J^{eq}}, \quad \epsilon_J \ll 1. \tag{22}$$

The maximum value of this parameter, say $\epsilon_{\max}$, characterizes the numerical error of the method, as due to lack of adiabaticity. Intuitively, large values of $\epsilon_{\max}$ indicate that the time step should be reduced, while small values carry the opposite message. Since we work at a constant mesh spacing, a change of the time step must necessarily involve a corresponding change of the discrete speeds, namely,

$$\vec{c}_i^{\,+} = \frac{\delta t^+}{\delta t}\vec{c}_i, \tag{23}$$

where $\vec{c}_i$ and $\vec{c}_i^{\,+}$ are the discrete velocities before and after the change of time step, respectively. The physical quantities must be continuous across the time interface, which means

$$T^+ = T, \quad \vec{J}^+ = \vec{J}. \tag{24}$$

This is not true for the sound speed. It is instructive to illustrate this point with a concrete example. Suppose the time step is increased by a factor 2, $\delta t^+ = 2\delta t$. Since δx remains constant, the particle speed $c = \delta x/\delta t$, as well as the sound speed, must be reduced by a factor of 2, i.e., the system is cooled down. The change of the physical quantities is as follows:

$$\delta t \to 2\delta t, \quad \delta x \to \delta x, \tag{25}$$

$$c_s \to c_s/2, \quad c \to c/2, \tag{26}$$

$$T \to T, \quad \vec{u} \to \vec{u}, \tag{27}$$

$$D_T \to D_T, \quad \omega_J^{-1} \to 4\omega_J^{-1} - \delta t. \tag{28}$$

The transformation law for ω_J follows from the invariance of the diffusivity $D_T = c_s^2(1/\omega_J - \delta t/2)$. The corresponding transformations of dimensionless quantities follow from the physical ones by recalling that space units stay unchanged, while the time units are doubled, from δt to $2\delta t$. Since the physical flow speed u stays unchanged, while the sound and molecular speeds are halved, the local equilibrium must change too. Indeed, the dimensionless group uc/c_s^2 entering the local equilibrium gets doubled, which means that the flow speed in lattice units u/c_s must increase by a factor of 2 when passing across the time interface. As a result

$$f_i^{eq,+} = f_i^{eq}(2u) = Tw_i(1 + \vec{c}_i \cdot \vec{u}/c_s^2). \tag{29}$$

However, for the present case of no-flow conditions, this point is immaterial.

As to nonequilibria, we impose

$$\delta t^+ \omega_J^+ f_i^{neq,+} = \delta t \omega_J f_i^{neq}, \tag{30}$$

which follows directly from the continuity of $\partial_t f$ across the time interface. The relations (29) and (30) provide the transformation law of the distribution function across the time interface.

We observe that increasing the time step is synonymous with cooling the system, and, conversely, reducing it is equivalent to heating up the system. Physically, this means that "fast" molecules are used when the dynamics is fast, and "slow" molecules are used when the dynamics is slow. Thus, the variable time step is literally associated with a dynamic *annealing procedure*. It should be noted that for problems with net fluid flow ($u \neq 0$), dynamic annealing is restricted by *realizability* conditions of the kinetic scheme, specifically by the requirements that local equilibria remain positive definite. However, for no-flow problems, such as the one considered here, this limitation is lifted [see Eq. (16)].

V. NUMERICAL SCHEME FOR THE PHASE-FIELD EQUATION

A simple explicit scheme for the phase-field and temperature equations is as follows:

$$d\phi = \frac{\xi^2 \delta t}{\tau} \bar{\Delta}\phi(t) - \delta t g_\phi(t) - \delta t \lambda p_\phi(t) \tilde{T}(t), \tag{31}$$

$$dT = \delta t D_T \bar{\Delta} T + \frac{L}{c_p} h_\phi(t) d\phi, \tag{32}$$

where $d\phi \equiv \phi(t+\delta t) - \phi(t)$, $dT = T(t+\delta t) - T(t)$, and $\bar{\Delta}$ is the discretized Laplacian, in our case, a nine-point template in order to reduce lattice anisotropy.

Larger time steps can be taken by replacing the right hand side of Eq. (32) with the kinetic scheme, that is, by solving the kinetic equation (11) instead of the scalar equation (32).

Latent heat production can be included in the kinetic equation by inserting the corresponding term in the expression of the local equilibria f^{eq}:

$$f_i^{eq} = w_i \left(T(t) + \frac{L}{c_p} h_\phi(t) d\phi \right). \tag{33}$$

The latent heat term may cause an instability, again due to violations of the realizability constraints, unless the time step is properly controlled. Strong heat production can result from a combination of serial solidification and melting processes in the transition region. This potential instability can be softened by using a semi-implicit time-marching scheme, instead of the explicit time marching, Eq. (31):

$$\phi(t+\delta t) - \phi(t) = \frac{\xi^2 \delta t}{\tau} \bar{\Delta}\phi(t) - \delta t g_\phi(t) + \delta t \lambda p_\phi(t) \times \left(\tilde{T}(t) + \frac{L}{c_p} h_\phi(t) d\phi \right).$$

This equation can be recast in explicit form as follows:

$$d\phi = \frac{(\xi^2/\tau)\bar{\Delta}\phi(t) - g_\phi(t) + \lambda p_\phi(t) \tilde{T}(t)}{1 + \lambda (L/c_p) h_\phi(t) p_\phi(t)} \delta t. \tag{34}$$

Clearly, the feedback term in the denominator acts as an effective limiter to $d\phi$ in the presence of strong latent heat effects.

VI. NUMERICAL RESULTS

The present kinetic scheme is validated through comparison with existing literature results for the problem of dendritic growth from a pure melt [1,5]. Initial conditions are as follows. The phase field is nonzero only around the origin, with a sharp transition around a nucleus radius r_0, $\phi(\vec{r},0) = \tanh[(r-r_0)/\xi\sqrt{2}]$. The temperature field is initialized accordingly, with a melting point temperature T_m in the solid nucleus, and boundary temperature T_0 elsewhere:

$$T(\vec{r},0) = \phi(\vec{r},0) T_m + [1 - \phi(\vec{r},0)] T_0. \tag{35}$$

Due to the fourfold symmetry of the problem, the simulation is confined to the first quarter only. Adiabatic (no-flux) conditions are imposed at the outer boundaries, $y = y_{\max}$ and $x = x_{\max}$, while specular symmetry is imposed at the inner ones, $x=0$ and $y=0$.

TABLE II. Dendritic growth. $\delta x = 0.4$, $\tau = 1$, $\xi = 1$.

St	ϵ	λ	D	Ca	$\tilde{v}$	$\tilde{v}_{\text{theor}}$	Size
0.55	0.05	4.70	2	0.277	0.0167	0.0170	300×800
0.55	0.05	7.05	3	0.185	0.0178	0.0170	200×600
0.45	0.05	9.40	4	0.139	0.00564	0.00545	400×1200
0.30	0.05	23.5	10	0.055	0.000685	0.00068	500×2000
0.55	0.02	4.70	2	0.277	0.00694	0.00685	300×1000

A. Dendritic growth with isotropic heat transfer

We first consider the transient evolution of a small nucleus placed in an undercooled melt. In the course of the evolution, the shape of the growing nucleus changes from round to dendritic, in a way that depends on the anisotropy of the surface tension and on the kinetic coefficient. After the transient dies out, the growing dendrite attains a stationary state, which is characterized by a constant value of the tip velocity and radius. Surface tension anisotropy is modeled by a standard fourfold symmetric expression [1,2]

$$\gamma(\vec{n}) = 1 - 3\epsilon_4 + 4\epsilon_4 \frac{(\nabla_x \phi)^4 + (\nabla_y \phi)^4}{|\vec{\nabla}\phi|^4}, \tag{36}$$

where $\vec{n} = (\cos\theta, \sin\theta)$ is the outward normal to the growing surface and ϵ_4 is the anisotropy parameter. In terms of the orientation angle

$$\gamma(\theta) = 1 + \epsilon_4 \cos 4\theta. \tag{37}$$

All simulations of dendritic growth were performed with infinite kinetics, $\mu^{-1} = 0$, which means the temperature on the interface is defined solely by the Gibbs-Thomson condition and does not depend on the tip speed V [see Eq. (5)]. This assumption allows one to derive λ and Ca from Eq. (6) in terms of the dimensionless ratio of phase to heat diffusivity, $D_T\tau/\xi^2$:

$$\lambda = \frac{a_2}{a_1} \frac{\tau D_T c_p}{\xi^2 L}, \quad \text{Ca} = \frac{a_2 \xi^2}{\tau D_T}, \tag{38}$$

namely, $\lambda = (\text{Ca}/a_1)(c_p/L)$.

The dendritic tip velocity, v, was measured and its dimensionless value $\tilde{v} = v d_0/D_T$ was compared with the theoretical one given by the equation of Nash and Glicksman (see [1]). As clearly shown in Table II, satisfactory agreement is obtained for all values of the parameters explored, including the most challenging ones (St=0.30, Ca=0.055).

The time evolution of the time step and the corresponding value of the *diabatic* control parameter ϵ are shown in Fig. 1.

It is seen that in the initial stage the time step stays close to its initial value ($dt_0/\tau = 10^{-3}$) because the tip speed is decreasing very fast (see Fig. 2). Once the tip speed stabilizes, the time step grows by over an order of magnitude, until it starts to decrease again when the tip speed shows a further

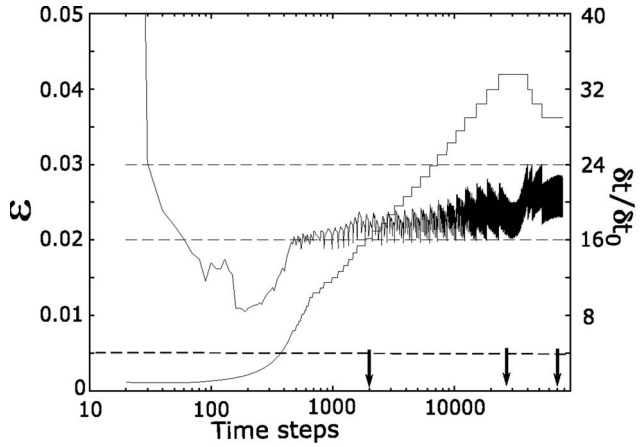

FIG. 1. Evolution of the diabatic parameter and time step vs number of time steps. The main parameters are St=0.30, Ca =0.055; see Table II. The upper two dashed lines correspond to the maximum and minimum allowed values of the diabatic parameter ϵ. The lower dashed line indicates the maximum time step allowed by the diffusive CFL condition for an explicit finite-difference method. The ratio of new to old time step is fixed: $dt^+/dt=1.05$.

increase toward its final steady-state value. Note that the product $\tilde{v}\delta t$ stays within a factor of 2 of its initial value, indicating that the time step adjusts itself to the changes of the tip speed rather than to a (constant) sound speed as in standard kinetic methods.

The morphological changes of the growing nucleus are displayed in Fig. 3, which reports three snapshots after 2000, 26 000, and 70 000 time steps, respectively (the three arrows at the bottom of Fig. 1). A comparison with the maximum time step allowed by a diffusive CFL condition, $\delta t_{CFL} = \delta x^2/2dD_T$ (d spatial dimensions), shows that the present method achieves almost an order of magnitude speedup. As an indication of computational performance, the simulation

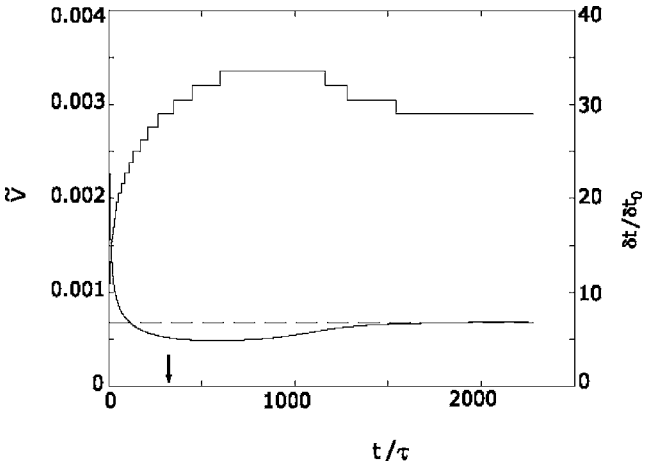

FIG. 2. Value of the tip velocity $\tilde{v}$ and time step vs dimensionless time. Not shown is the initial value $\tilde{v}(0)=0.012$. The parameters are the same as in Fig. 1. The dashed line corresponds to the theoretical value of the steady-state tip speed. The stepped curve reports the ratio of actual to initial time step. The arrow indicates the maximum time span allowed by the diffusive CFL condition, with the same number of time steps.

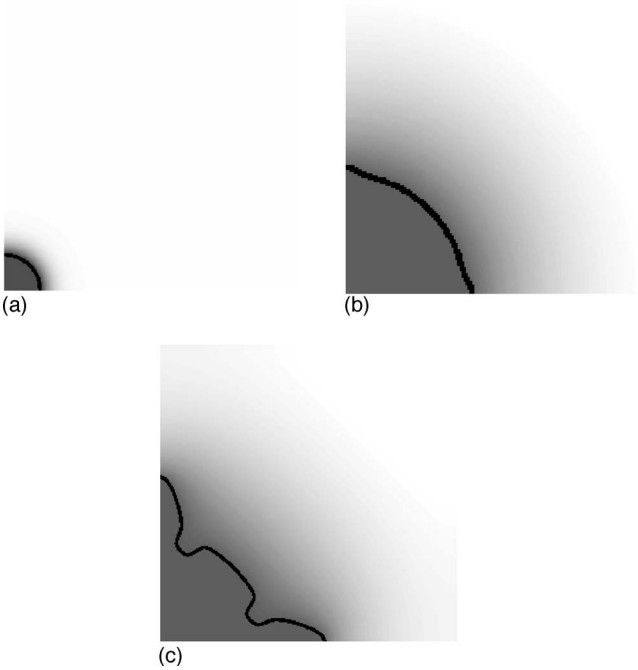

FIG. 3. Screen shots of the phase field for the case St=0.30 and Ca=0.05 (see Table II), after 2000, 26 000, and 70 000 time steps. Dark color codes for high temperature. The thick line shows the shape of the interface.

of 75 000 time steps on a 1000×1000 grid, for the case St =0.30 and Ca=0.055, takes about 2 h CPU time on a 2.4 GHz Pentium Xeon processor.

B. Dendritic growth with anisotropic heat conductivity in the liquid

In the next set of simulations, we investigate the influence of anisotropy of the heat conductivity on the resulting orientation of the dendritic tip. Heat conduction properties of materials are normally isotropic, although there are number of notable exceptions. For instance, in single crystals, heat conduction properties depend on the crystallographic grid, and that is why they can be anisotropic even though the melt properties are normally isotropic. Other examples are liquid crystals, which exhibit anisotropic heat conduction in the liquid phase (see, e.g., [15]). The heat equation in the anisotropic case takes the form

$$\partial_t T = \nabla_\alpha (D^T_{\alpha\beta} \nabla_\beta T),$$

where $D^T_{\alpha\beta}$ is the heat diffusivity tensor. This tensor can be defined through the maximum and minimum values of the heat conductivity and the angle between maximum diffusion direction and x axis, $D^T_{\max}$, $D^T_{\min}$, and χ, respectively,

$$D^T_{\alpha\beta} = \begin{pmatrix} D^T_{\max} - D^T_\Delta \sin^2(\chi) & -\frac{1}{2} D^T_\Delta \sin(2\chi) \\ -\frac{1}{2} D^T_\Delta \sin(2\chi) & D^T_{\max} - D^T_\Delta \cos^2(\chi) \end{pmatrix},$$

where $D^T_\Delta \equiv D^T_{\max} - D^T_{\min}$.

Crystal growth for the standard case of a fourfold anisotropy in the surface tension is simulated jointly with an

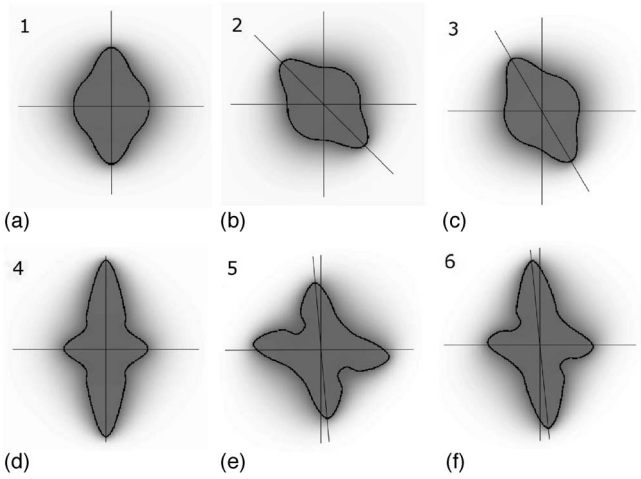

FIG. 4. Dendritic growth with anisotropic surface tension and heat conduction. Cases 1–3 and 4–6 correspond to $\epsilon=0.00$ and 0.005 respectively. In all cases χ equals 0°, −45°, −60°. Main parameters are St=0.55, $\tau=1$, $\lambda=9.40$. The domain size is 600 × 600, with $\xi=1.0$ and $dx=0.4$.

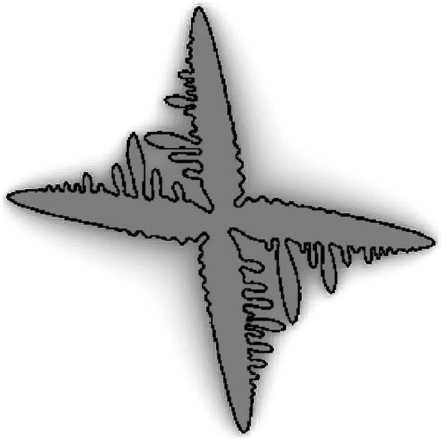

FIG. 5. Snapshot of dendritic growth with anisotropic heat conduction after 25 000 time steps. Major parameters are St=0.55, $\tau=1$, $\lambda=14.1$, $\epsilon=0.05$, and $\xi=45°$. The domain size is 2500 × 2500, with a mesh spacing $dx=0.6$ and width $w=1.0$.

(equally) anisotropic heat conduction for both liquid and solid phases. In the Fig. 4 different shapes are shown corresponding to different orientations of $D^T_{\max}$. For every orientation angle, two simulations, with and without anisotropy in the surface tension, are presented. The case with isotropic surface tension shows preferential growth along the directions given by the heat orientation angle, that is, $\chi=0$, −45°, −60°, respectively. Once anisotropy in the surface tension is switched on (lower row), the picture becomes significantly more complex due to the nonlinear interaction between heat and surface tension anisotropy. Indeed, when both anisotropies are on, preferential growth takes place along new directions, which do not coincide with the specified values of either θ or χ.

Next, we show that computation of sidebranching (growth of secondary dendrites) is possible within reasonable time. Here we present a calculation for case 5 (see Fig. 4) with $\chi=-45°$, shown in Fig. 5, corresponding to 25 000 time steps. The result was observed in about 4.5 h CPU time on a 2.4 GHz Pentium processor. The sidebranching was induced by a space-time random perturbation in the coupling coefficient; $\delta\lambda/\lambda=0.05$ is used. The effects of anisotropic diffusivity on the the primary dendrites, which grow slightly slanted with respect to the Cartesian axes, are clearly visible. On the other hand, preferential heat transfer at $\chi=-45°$ results in secondary dendrites growing only in the second and fourth quadrants. These results witness the major impact of anisotropic surface tension and heat transport properties on the complex morphology of the growing crystal.

C. Dendritic growth with small undercooling using a block-structured grid

Simulations for small undercoolings are challenging because the temperature field is long ranged compared to the length scale of the crystal. Different attempts have been made in order to reduce computational costs. Karma and Plapp introduced a random walker for the computation of heat transport [16]. Provatas *et al.* [17] made use of an adaptive grid when calculating dendritic growth for an undercooling of St=0.25 and 0.1.

We adapted the concept introduced by Filippova and Hänel [18] to set up a block-structured grid with a fine grid in the region of the phase transition and a coarse grid far away. In the beginning it is not known how large the domain should be for a certain set of parameters to mimic an infinitely large domain as it is assumed in the derivation of the analytic solution. Therefore, we start with the domain of the finest grid only. In this domain the dendritic growth takes place and the phase-field equation is solved. The initial temperature in the domain is set according to the chosen undercooling: $T_{\text{init}}=\text{St}L/c_p$. We apply zero-flux boundary conditions at the boundaries of the current computational domain and measure the temperature T_{test} at the cut of the boundary and the axis of the growing tip. Whenever T_{test} is larger than a critical value T_{crit} a new layer of a coarser grid is dynamically added. Every additional layer consists of three subdomains where two subdomains have a coarsening factor $n=2$. The resulting grid hierarchy for two additional layers can be seen in Fig. 6. The temperature in the added layer is set to T_{init}.

The relaxation matrix is different in the different layer grids due to the relations (15) and (19). In particular, we kept the speed of sound c_s the same in every layer by changing the time step from layer to layer by the same factor as the grid spacing. Therefore, we have different time steps δt in the different layers and the relaxation parameter ω_J is also different according to Eq. (19). On the finest grid (layer 0) there is the smallest time step and this serves as the clock for the whole domain. In the next layer (layer 1) we need to perform computations only every second clock time, in layer 2 only every fourth clock time, and so on.

In order to have the same scalar value on all layers the distribution functions at the interfaces between two layers are rescaled via

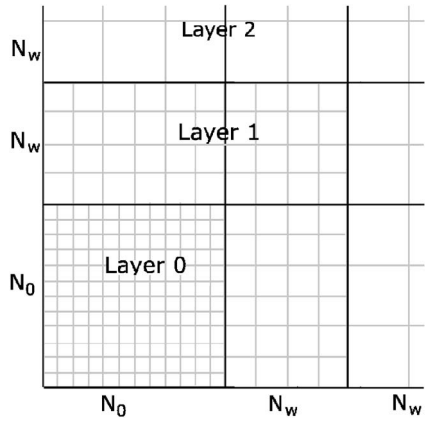

FIG. 6. Block-structured grid. Phase-field equations are solved only on the finest grid. Heat transport is computed everywhere.

$$f_i^c(\vec{r},t) = f_i^f(\vec{r},t)\frac{\omega_J^f}{\omega_J^c} + f_i^{eq,f}(\vec{r},t)\left(1 - \frac{\omega_J^f}{\omega_J^c}\right), \tag{39}$$

$$f_i^f(\vec{r},t) = \tilde{f}_i^c(\vec{r},t)\frac{\omega_J^c}{\omega_J^f} + \tilde{f}_i^{eq,c}(\vec{r},t)\left(1 - \frac{\omega_J^c}{\omega_J^f}\right), \tag{40}$$

where the superscripts c and f indicates the coarse and fine grids, respectively. The tilde denotes time and space interpolation. In particular, we used a linear interpolation in both space and time. The rescaling is performed after the collision step. The same type of rescaling has been derived by Dupuis and Chopard for the lattice Bhatnagar-Gross-Krook (LBGK) method [19].

In order to keep the dendritic tip inside layer 0 the computational domain moves with the advancing solidification front. Once the two tips were grown from the original seed we are only interested in the evolution of the tip along the y direction. In every time step we check whether the y coordinate of the tip exceeds some value. Everything within $y \leqslant n\delta x_0$ is chopped off, where δx_0 is the grid spacing in layer 0 and n is an integer. Because we want to keep the entire size of every layer we have to perform a mapping for the distribution functions, which is done by a bilinear interpolation. In all our computations we set $n=1$.

Figure 7 shows the simulation results for St=0.25 and 0.1.

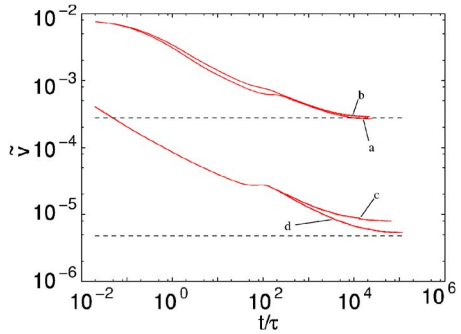

FIG. 7. (Color online) Tip velocity $\tilde{v}$ versus time for St=0.25 (curves a and b) and St=0.1 (curves c and d). The parameters of the calculations are found in Table III.

TABLE III. Simulation with small undercooling.

	St	D	N_0	N_w	δx	$\delta t_{\max}$	$\tilde{v}$	$\tilde{v}_{\text{theor}}$
a	0.25	13	301	50	0.4	0.037	0.000270	0.00028
b	0.25	13	401	50	0.6	0.088	0.000285	0.00028
c	0.1	80	301	50	0.6	0.041	0.0000080	0.0000048
d	0.1	80	801	50	0.6	0.041	0.0000051	0.0000048

The results and simulation parameters are summarized in Table III. For both undercoolings we chose the temperature $T_{crit}=(\text{St}-10^{-6})L/c_p$ as the criterion for adding a new layer. In the final situation we had five layers in total for St=0.25 and eight for St=0.1. The latter needed about 22 h on a 2.4 GHz Pentium processor.

D. Preliminary three-dimensional results

The present kinetic method readily extends to three-dimensional situations. Leaving full details to a future publication, here we only sketch the basic points. The three-dimensional scheme requires six distribution functions, associated with the corresponding six nearest-neighbor discrete speeds:

$$c_1 = (1,0,0), \quad c_2 = (0,1,0), \quad c_3 = (0,0,1),$$

$$c_4 = (-1,0,0), \quad c_5 = (0,-1,0), \quad c_6 = (0,0,-1).$$

The corresponding 6×6 collision matrix reads as follows:

$$\Omega = \frac{1}{2}\begin{bmatrix} \Lambda & -\Lambda \\ -\Lambda & \Lambda \end{bmatrix} + \begin{bmatrix} P & P \\ P & P \end{bmatrix}, \quad P \equiv \frac{1}{6\delta t}\begin{pmatrix} 2 & -1 & -1 \\ -1 & 2 & -1 \\ -1 & -1 & 2 \end{pmatrix}, \tag{41}$$

where Λ relates to the heat conduction tensor through the following expression [7]:

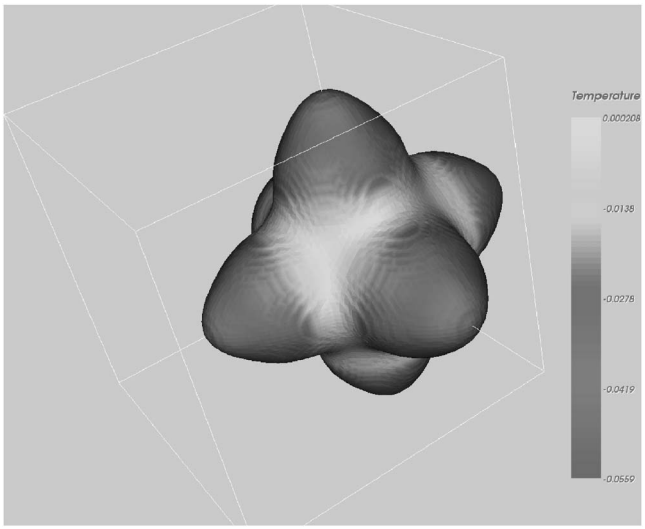

FIG. 8. Shape of the 3D dendritic crystal for the case St $=0.45$, Ca$=0.22$, $\epsilon_4^*=0.015$, $D=3$. The grid size is $250\times 250\times 250$ grid points with a mesh spacing $\delta x=0.6$, $\xi=1.0$.

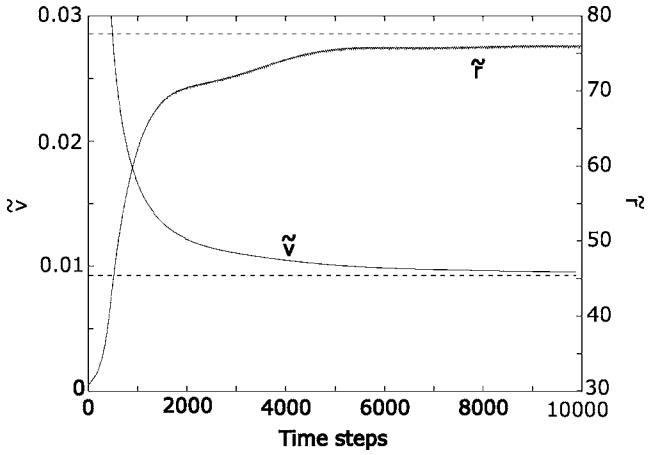

FIG. 9. Tip velocity and tip radius vs time steps. $St=0.45$, $\delta_x=0.6$, $\epsilon_4^*=0.015$, $D=3$, size $200\times200\times300$.

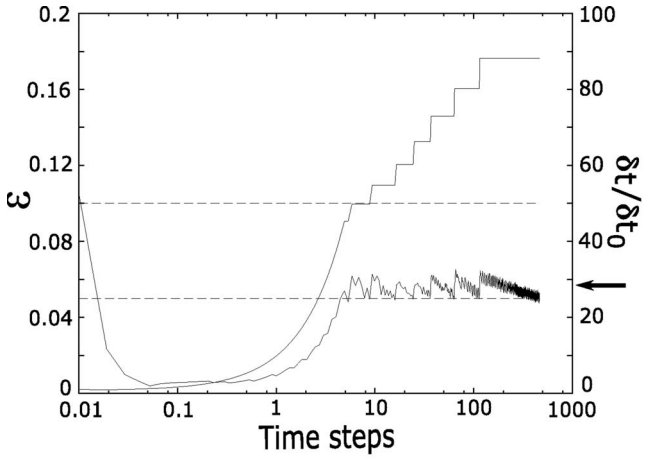

FIG. 10. Tip velocity and tip radius vs time steps. $St=0.45$, $\delta_x=0.6$, $\epsilon_4^*=0.015$, $D=3$, size $250\times250\times250$. The arrow indicates the maximum step allowed by the diffusive CFL condition.

$$\Lambda_{\alpha\beta}=\frac{1}{\delta t}\left(2D_{\alpha\beta}+\frac{1}{2}\delta_{\alpha\beta}\right)^{-1}_{\alpha\beta}. \tag{42}$$

The matrix P can be shown to ensure better stability and isotropy of the scheme [7].

The surface tension is a straightforward generalization of the two-dimensional expression, namely,

$$\gamma(\vec{n})=\gamma_0\left(1-3\epsilon_4+4\epsilon_4\frac{(\nabla_x\phi)^4+(\nabla_y\phi)^4+(\nabla_z\phi)^4}{|\vec{\nabla}\phi|^4}\right). \tag{43}$$

By symmetry arguments, only one-eighth of the whole crystal was simulated. Figure 8 shows the crystal surface of the three-dimensional dendrite. The shading corresponds to the local temperature (light=hot, dark=cold). The cold regions on the tips indicate the influence of the Gibbs-Thomson effect, which makes low-curvature surfaces hotter than high-curvature ones. The evolutions of the tip velocity and radius are plotted in Fig. 9. Here $\tilde{r}$ is defined as $\tilde{r}\equiv r/d_0$.

The time-adaptive procedure proceeds exactly in the same way as in the 2D case. The evolution of the time step during the growth process is plotted in Fig. 10. From this figure, it is seen that the error estimate goes below the minimum value at the end of simulation. This means that the time step is not limited by the kinetic scheme, but rather by the semi-implicit time marching for the phase-field equation. Note that the time step is almost a factor of 3 larger than the maximum diffusive time step for the central-finite-difference method.

The simulation of 6000 time steps on a 250^3 grid required about 24 h CPU time on a 2.4 GHz Pentium processor.

VII. CONCLUSIONS

Summarizing, we have presented a kinetic scheme that permits the solution of phase-field equations, coupled with temperature dynamics, using an explicit time-marching schedule free of diffusive CFL constraints. At variance with standard kinetic schemes, the present one can adapt the time step to the actual dynamics of the growth process, thus resulting in substantial CPU-time savings. The scheme has been validated for a variety of growth phenomena, including two-dimensional dendritic growth from the melt, for both isotropic and nonisotropic surface tension and heat diffusivity. A preliminary application to three-dimensional dendritic growth has also been presented.

ACKNOWLEDGMENTS

S.S. is grateful to the Alexander von Humboldt Foundation for financial support. He also wishes to acknowledge kind hospitality at the Institute for Crystal Growth, Berlin, where this work was performed.

[1] A. Karma and W.-J. Rappel, Phys. Rev. E **57**, 4323 (1998).
[2] G. B. McFadden, A. A. Wheeler, R. J. Braun, S. R. Coriell, and R. F. Sekerka, Phys. Rev. E **48**, 2016 (1993).
[3] X. Tong, C. Beckermann, A. Karma, and Q. Li, Phys. Rev. E **63**, 061601 (2001).
[4] C. W. Lan, C. M. Hsu, C. C. Liu, and Y. C. Chang, Phys. Rev. E **65**, 061601 (2002).
[5] Y.-T. Kim, N. Provatas, N. Goldenfeld, and J. Dantzig, Phys. Rev. E **59**, R2546 (1999).
[6] G. Caginalp and W. Xie, Arch. Ration. Mech. Anal. **142**, 293 (1998).
[7] I. Rasin, S. Succi, and W. Miller, J. Comput. Phys. **206**, 453 (2005).
[8] D. Wolf-Gladrow, *Lattice-Gas Cellular Automata and Lattice Boltzmann Models* (Springer, Berlin, 2000).
[9] D. Raabe, Modell. Simul. Mater. Sci. Eng. **12**, R13 (2004).

[10] O. Penrose and P. C. Fife, Physica D **43**, 44 (1990).
[11] F. Higuera, S. Succi, and R. Benzi, Europhys. Lett. **9**, 345 (1989).
[12] R. Benzi, S. Succi, and M. Vergassola, Phys. Rep. **222**, 145 (1992).
[13] R. G. M. van der Sman and M. H. Ernst, J. Stat. Phys. **94**, 766 (1999).
[14] M. Bouzidi, D. d'Humières, P. Lallemand, and L.-S. Luo, J. Comput. Phys. **172**, 704 (2001).
[15] R. González-Cinca, L. Ramírez-Piscina, J. Casademunt, A. Hernández-Machado, T. Tóth-Katona, T. Börzsönyi, and Á. Buka, J. Cryst. Growth **193**, 712 (1998).
[16] Mathis Plapp and Alain Karma, J. Comput. Phys. **165**, 592 (2000).
[17] N. Provatas, N. Goldenfeld, and J. Dantzig, J. Comput. Phys. **148**, 265 (1999).
[18] O. Filippova and D. Hänel, J. Comput. Phys. **147**, 219 (1998).
[19] Alexandre Dupuis and Bastien Chopard, Phys. Rev. E **67**, 066707 (2003).